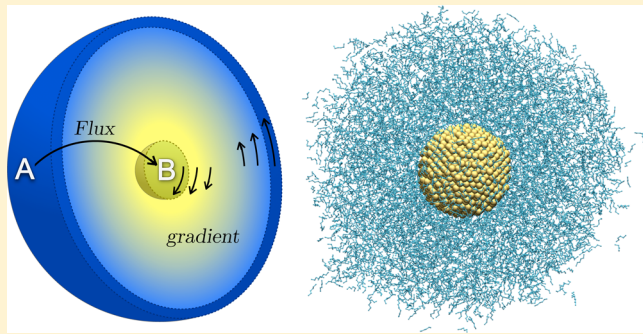


A Method for Creating Thermal and Angular Momentum Fluxes in Nonperiodic Simulations

Kelsey M. Stocker and J. Daniel Gezelter*

Department of Chemistry and Biochemistry, University of Notre Dame, 251 Nieuwland Science Hall, Notre Dame, Indiana 46556, United States

ABSTRACT: We present a new reverse nonequilibrium molecular dynamics method that can be used with nonperiodic simulation cells. This method applies thermal and/or angular momentum fluxes between two arbitrary regions of the simulation and is capable of creating stable temperature and angular velocity gradients while conserving total energy and angular momentum. One particularly useful application is the exchange of kinetic energy between two concentric spherical regions, which can be used to generate thermal transport between nanoparticles and the solvent that surrounds them. The rotational couple to the solvent (a measure of interfacial friction) is also available via this method. As tests of the new method, we have computed the thermal conductivities of gold nanoparticles and water clusters, the interfacial thermal conductivity (G) of a solvated gold nanoparticle, and the interfacial friction of a variety of solvated gold nanostructures.



1. INTRODUCTION

Nonequilibrium molecular dynamics (NEMD) methods impose a temperature or velocity *gradient* on a system,^{1–14} and use linear response theory to connect the resulting thermal or momentum *flux* to transport coefficients of bulk materials,

$$j_z(p_x) = -\eta \frac{\partial v_x}{\partial z}, \quad J_z = \lambda \frac{\partial T}{\partial z} \quad (1)$$

Here, $\partial T/\partial z$ and $\partial v_x/\partial z$ are the imposed thermal and momentum gradients, and as long as the imposed gradients are relatively small, the corresponding fluxes, J_z and $j_z(p_x)$, have a linear relationship to the gradients. The coefficients that provide this relationship correspond to physical properties of the bulk material, either the shear viscosity (η) or thermal conductivity (λ). For systems which include phase boundaries or interfaces, however, it is often unclear what gradient (or discontinuity) should be imposed at the boundary between materials.

In contrast, reverse nonequilibrium molecular dynamics (RNEMD) methods impose an unphysical *flux* between different regions or “slabs” of the simulation box.^{15–23} The system responds by developing a temperature or velocity *gradient* between the two regions. The gradients which develop in response to the applied flux have the same linear response relationships to the transport coefficient of interest. Since the amount of the applied flux is known exactly, and measurement of a gradient is generally less complicated, imposed-flux methods typically take shorter simulation times to obtain converged results. At interfaces, the observed gradients often exhibit near-discontinuities at the boundaries between dissimilar materials. RNEMD methods do not need many trajectories

to provide information about transport properties, and they have become widely used to compute thermal and mechanical transport in both homogeneous liquids and solids^{15,16,19} as well as heterogeneous interfaces.^{17,18,20–23}

The strengths of specific algorithms for imposing the flux between two different slabs of the simulation cell has been the subject of some renewed interest. The original RNEMD approach used kinetic energy or momentum exchange between particles in the two slabs, either through direct swapping of momentum vectors or via virtual elastic collisions between atoms in the two regions. There have been recent methodological advances which involve scaling all particle velocities in both slabs.^{20,22} Constraint equations can be simultaneously imposed to require the simulation to conserve both total energy and total linear momentum. The most recent and simplest of the velocity scaling approaches allows for simultaneous shearing (to provide viscosity estimates) as well as scaling (to provide information about thermal conductivity).²²

The primary method of studying heat transfer at curved nanoscale interfaces has involved transient nonequilibrium molecular dynamics and temperature relaxation.²⁴ Recently, RNEMD has been used to generate heat fluxes between the curved surfaces of nanotubes and polyamide-6,6 surroundings in nanocomposites,²⁵ and the thermal conductivity was inferred using a quasi-one-dimensional version of Fourier’s law.

RNEMD methods to generate *momentum* flux have only been used in periodic simulation cells where the exchange regions are physically separated along one of the axes of the

Received: March 15, 2014

Published: April 16, 2014

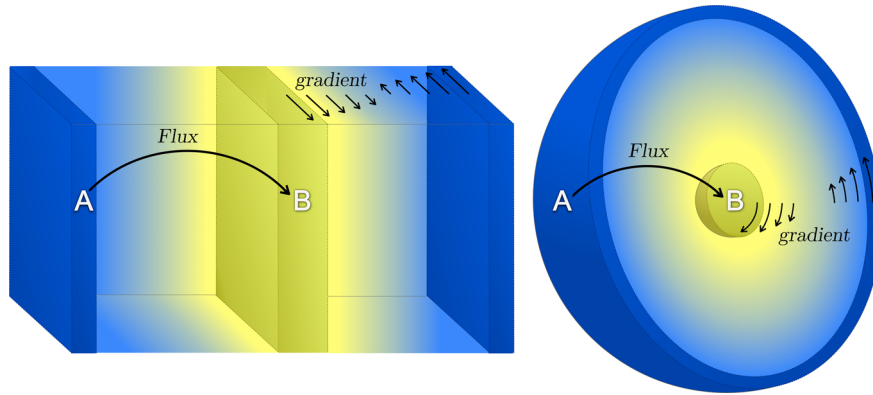


Figure 1. Schematics of periodic (left) and nonperiodic (right) velocity shearing and scaling RNEMD. A kinetic energy or momentum flux is applied from region A to region B. Thermal gradients are depicted by a color gradient. Linear or angular velocity gradients are shown as arrows.

simulation cell. This limits the applicability to infinite planar interfaces which are perpendicular to the applied flux. In order to model steady-state nonequilibrium distributions for curved surfaces (e.g., rotating nanoparticles in contact with counter-rotating solvent), or for regions that are not planar slabs, the method requires some generalization. In the following sections, we present a new velocity shearing and scaling (VSS) RNEMD algorithm which has been explicitly designed for nonperiodic simulations and use the method to compute some thermal transport and solid–liquid friction at the surfaces of spherical and ellipsoidal nanoparticles.

2. VELOCITY SHEARING AND SCALING FOR NONPERIODIC SYSTEMS

The original periodic VSS-RNEMD approach uses a series of simultaneous velocity shearing and scaling exchanges between the two slabs.²² This method imposes energy and linear momentum conservation constraints while simultaneously creating a desired flux between the two slabs. These constraints ensure that all configurations are sampled from the same microcanonical (*NVE*) ensemble.

We have extended the VSS method for use in *nonperiodic* simulations, in which the “slabs” have been generalized to two separated regions of space. These regions could be defined as concentric spheres (as in Figure 1), or one of the regions can be defined in terms of a dynamically changing “hull” comprising the surface atoms of the cluster. This latter definition is identical to the hull used in the Langevin Hull algorithm.²⁶ For the nonperiodic variant, the constraints fix both the total energy and total *angular* momentum of the system while simultaneously imposing a thermal and angular momentum flux between the two regions.

After a time interval of Δt , the particle velocities (\mathbf{v}_i and \mathbf{v}_j) in the two shells (A and B) are modified by a velocity scaling coefficient (a and b) and by a rotational shearing term (\mathbf{c}_a and \mathbf{c}_b). The scalars a and b collectively provide a thermal exchange between the two regions. One of the values is larger than 1, and the other, smaller. To conserve total energy and angular momentum, the values of these two scalars are coupled. The vectors (\mathbf{c}_a and \mathbf{c}_b) provide a relative rotational shear to the velocities of the particles within the two regions, and these vectors must also be coupled to constrain the total angular momentum.

Once the values of the scaling and shearing factors are known, the velocity changes are applied,

scaling

$$\begin{aligned} \mathbf{v}_i &\leftarrow a(\mathbf{v}_i - \langle \omega_a \rangle \times \mathbf{r}_i) + \mathbf{c}_a \times \mathbf{r}_i \\ \mathbf{v}_j &\leftarrow b(\mathbf{v}_j - \langle \omega_b \rangle \times \mathbf{r}_j) + \mathbf{c}_b \times \mathbf{r}_j \end{aligned}$$

Here $\langle \omega_a \rangle$ and $\langle \omega_b \rangle$ are the instantaneous angular velocities of each shell, and \mathbf{r}_i is the position of particle i relative to a fixed point in space (usually the center of mass of the cluster). Particles in the shells also receive an additive “angular shear” to their velocities. The amount of shear is governed by the imposed angular momentum flux, $j_r(\mathbf{L})$,

$$\mathbf{c}_a = -j_r(\mathbf{L}) \cdot \tilde{\mathbf{I}}_a^{-1} \Delta t + \langle \omega_a \rangle \quad (2)$$

$$\mathbf{c}_b = +j_r(\mathbf{L}) \cdot \tilde{\mathbf{I}}_b^{-1} \Delta t + \langle \omega_b \rangle \quad (3)$$

where $\tilde{\mathbf{I}}_{\{a,b\}}$ is the moment of inertia tensor for each of the two shells.

To simultaneously impose a thermal flux (J_r) between the shells, we use energy conservation constraints,

$$K_a - J_r \Delta t = a^2 \left(K_a - \frac{1}{2} \langle \omega_a \rangle \cdot \tilde{\mathbf{I}}_a \cdot \langle \omega_a \rangle \right) + \frac{1}{2} \mathbf{c}_a \cdot \tilde{\mathbf{I}}_a \cdot \mathbf{c}_a \quad (4)$$

$$K_b + J_r \Delta t = b^2 \left(K_b - \frac{1}{2} \langle \omega_b \rangle \cdot \tilde{\mathbf{I}}_b \cdot \langle \omega_b \rangle \right) + \frac{1}{2} \mathbf{c}_b \cdot \tilde{\mathbf{I}}_b \cdot \mathbf{c}_b \quad (5)$$

Simultaneous solution of these quadratic formulas for the scaling coefficients, a and b , will ensure that the simulation samples from the original microcanonical (*NVE*) ensemble. Here $K_{\{a,b\}}$ is the instantaneous translational kinetic energy of each shell. At each time interval, we solve for a , b , \mathbf{c}_a and \mathbf{c}_b , subject to the imposed angular momentum flux, $j_r(\mathbf{L})$, and kinetic energy flux, J_r values. The new particle velocities are computed, and the simulation continues. System configurations after the transformations have exactly the same energy (and angular momentum) as before the moves.

As the simulation progresses, the velocity transformations can be performed on a regular basis, and the system will develop a temperature and/or angular velocity gradient in response to the applied flux. By fitting the radial temperature gradient, it is straightforward to obtain the bulk thermal conductivity,

$$J_r = -\lambda \left(\frac{\partial T}{\partial r} \right) \quad (6)$$

from the radial kinetic energy flux (J_r) that was applied during the simulation. In practice, it is significantly easier to use the integrated form of Fourier's law for spherical geometries. In sections 3.3–3.5 we outline ways of obtaining interfacial transport coefficients from these RNEMD simulations.

3. COMPUTATIONAL DETAILS

The new VSS-RNEMD methodology for nonperiodic system geometries has been implemented in our group molecular dynamics code, OpenMD.^{27,28} We have tested the new method to calculate the thermal conductance of a gold nanoparticle and SPC/E water cluster and compared the results with previous bulk RNEMD and experimental values. We have also investigated the interfacial thermal conductance and interfacial rotational friction for gold nanostructures solvated in hexane as a function of nanoparticle size and shape.

3.1. Force Fields. Gold–gold interactions are described by the quantum Sutton–Chen (QSC) model.²⁹ The QSC parameters are tuned to experimental properties such as density, cohesive energy, and elastic moduli and include zero-point quantum corrections.

The SPC/E water model³⁰ is particularly useful for validation of conductivities and shear viscosities. This model has been used to previously test other RNEMD and NEMD approaches, and there are reported values for thermal conductivities and shear viscosities at a wide range of thermodynamic conditions that are available for direct comparison.^{20,31}

Hexane molecules are described by the TraPPE united atom model,³² which provides good computational efficiency and reasonable accuracy for bulk thermal conductivity values. In this model, sites are located at the carbon centers for alkyl groups. Bonding interactions, including bond stretches and bends and torsions, were used for intramolecular sites closer than three bonds. For nonbonded interactions, Lennard-Jones potentials were used. We have previously utilized both united-atom (UA) and all-atom (AA) force fields for thermal conductivity,^{21–23} and since the united-atom force fields cannot populate the high-frequency modes that are present in AA force fields, they appear to work better for modeling thermal conductance at metal/ligand interfaces.

Gold–hexane nonbonded interactions are governed by pairwise Lennard-Jones parameters derived from Vlugt et al.³³ They fitted parameters for the interaction between Au and CH_x pseudoatoms based on the effective potential of Hautman and Klein for the Au(111) surface.³⁴

3.2. Simulation Protocol. In all cases, systems were equilibrated under nonperiodic isobaric–isothermal (NPT) conditions—using the Langevin Hull methodology²⁶—before any nonequilibrium methods were introduced. For heterogeneous systems, the gold nanoparticles and ellipsoids were created from a bulk fcc lattice and were thermally equilibrated before being solvated in hexane. Packmol³⁵ was used to solvate previously equilibrated gold nanostructures within a spherical droplet of liquid hexane.

Once equilibrated, thermal or angular momentum fluxes were applied for 1–2 ns, until stable temperature or angular velocity gradients had developed. Systems containing liquids were run under moderate pressure (5 atm) and temperatures (230 K) to avoid the formation of a vapor layer at the boundary of the cluster. Pressure was applied to the system via the nonperiodic Langevin Hull.²⁶ However, coupling to the external temperature and pressure bath was removed to avoid interference with the imposed RNEMD flux.

Because the method conserves *total* angular momentum, systems which contain a metal nanoparticle embedded in a significant volume of solvent will still experience nanoparticle diffusion inside the solvent droplet. To aid in computing the interfacial transport properties in these systems, a single gold atom at the origin of the coordinate system was assigned a mass 10,000 times its original mass. The bonded and nonbonded interactions for this atom remain unchanged, and the heavy atom is excluded from the RNEMD exchanges. The only effect of this gold atom is to effectively pin the nanoparticle at the origin of the coordinate system, while still allowing for any desired rotation about a given axis. For rotation of the gold ellipsoids we added two of these heavy atoms along the axis of rotation, separated by an equal distance from the origin of the coordinate system. These heavy atoms prevent off-axis tumbling of the nanoparticle and allow for measurement of rotational friction relative to a particular axis of the ellipsoid.

Angular velocity data were collected for the heterogeneous systems after a brief period of imposed flux to initialize rotation of the solvated nanostructure. Doing so ensures that we overcome the initial static friction and calculate only the dynamic interfacial rotational friction.

3.3. Thermal Conductivities. To compute the thermal conductivities of bulk materials, the integrated form of Fourier's law of heat conduction in radial coordinates can be used to obtain an expression for the heat transfer rate between concentric spherical shells:

$$q_r = -\frac{4\pi\lambda(T_b - T_a)}{\frac{1}{r_a} - \frac{1}{r_b}} \quad (7)$$

The heat transfer rate, q_r , is constant in spherical geometries, while the heat flux, J_r , depends on the surface area of the two shells. λ is the thermal conductivity, and $T_{a,b}$ and $r_{a,b}$ are the temperatures and radii of the two concentric RNEMD regions, respectively.

A kinetic energy flux is created using VSS-RNEMD moves, and the temperature in a set of 2 Å thick radial shells is recorded. The resulting temperature profiles are analyzed to yield information about the interfacial thermal conductance. As the simulation progresses, the VSS moves are performed on a regular basis, and the system develops a thermal or velocity gradient in response to the applied flux. Once a stable thermal gradient has been established between the two regions, the thermal conductivity, λ , can be calculated using a linear regression of the thermal gradient, $\langle dT/dr \rangle$:

$$\lambda = \frac{r_a}{r_b} \frac{q_r}{4\pi \left\langle \frac{dT}{dr} \right\rangle} \quad (8)$$

The rate of heat transfer, q_r , between the two RNEMD regions is easily obtained from either the applied kinetic energy flux and the area of the smaller of the two regions, or from the total amount of transferred kinetic energy and the run time of the simulation.

$$q_r = J_r \cdot A = \frac{\Delta KE}{\Delta t} \quad (9)$$

3.3.1. Thermal Conductivity of Nanocrystalline Gold. Calculated values for the thermal conductivity of a 40 Å radius gold nanoparticle (15,707 atoms) at a range of kinetic energy flux values are shown in Table 1. For these calculations, the hot

and cold slabs were excluded from the linear regression of the thermal gradient.

Table 1. Calculated Thermal Gradients of a Crystalline Gold Nanoparticle of Radius 40 Å Subject to a Range of Applied Kinetic Energy Fluxes^a

J_r (kcal/(fs·Å ²))	$\langle dT/dr \rangle$ (K/Å)
3.25×10^{-6}	0.114
6.50×10^{-6}	0.232
1.30×10^{-5}	0.449
3.25×10^{-5}	1.180
6.50×10^{-5}	2.339

^a Calculations were performed at an average temperature of 300 K. Gold–gold interactions are described by the quantum Sutton–Chen potential.

The measured thermal gradients $\langle dT/dr \rangle$ are linearly dependent on the applied kinetic energy flux J_r . The calculated thermal conductivity value, $\lambda = 1.004 \pm 0.009$ W/(m·K) compares well with previous bulk QSC values of 1.08–1.26 W/(m·K),²⁰ though still significantly lower than the experimental value of 320 W/(m·K), as the QSC force field neglects the significant electronic contributions to thermal conductivity. We note that there is only a minimal effect on the computed thermal conductivity of gold when comparing periodic (bulk) simulations carried out at the same densities as those used here.

3.3.2. Thermal Conductivity of an SPC/E Water Droplet. Calculated values for the thermal conductivity of a cluster of 6912 SPC/E water molecules were computed with a range of applied kinetic energy fluxes. As with the gold nanoparticle, the measured slopes were linearly dependent on the applied kinetic energy flux J_r , and the RNEMD regions were excluded from the $\langle dT/dr \rangle$ fit (see Figure 2).

The computed mean value of the thermal conductivity, $\lambda = 0.884 \pm 0.013$ W/(m·K), compares well with previous nonequilibrium molecular dynamics simulations of bulk SPC/E that were carried out in periodic geometries.^{36,37} These simulations gave conductivity values from 0.81–0.87 W/(m·K), and all of the simulated values are approximately 30–45% higher than the experimental thermal conductivity of water, which has been measured at 0.61 W/(m·K).³⁸

3.4. Interfacial Thermal Conductance. The interfacial thermal conductance, G , of a heterogeneous interface located at r_0 can be understood as the change in thermal conductivity in a direction normal (\hat{n}) to the interface,

$$G = (\nabla \lambda \cdot \hat{n})_{r_0} \quad (10)$$

For heterogeneous systems such as the solvated nanoparticle shown in Figure 3, the interfacial thermal conductance at the surface of the nanoparticle can be determined using a kinetic energy flux applied using the RNEMD method developed above.

In spherical geometries, it is most convenient to begin by finding the Kapitza or interfacial thermal resistance for a thin spherical shell,

$$R_K = \frac{1}{G} = \frac{\Delta T}{J_r} \quad (11)$$

where ΔT is the temperature drop from the interior to the exterior of the shell. For two concentric shells, the kinetic energy flux (J_r) is not the same (as the surface areas are not the same), but the heat transfer rate, $q_r = J_r A$, is constant. The thermal resistance of a shell with interior radius r is most conveniently written as

$$R_K = \frac{4\pi r^2 \Delta T}{q_r} \quad (12)$$

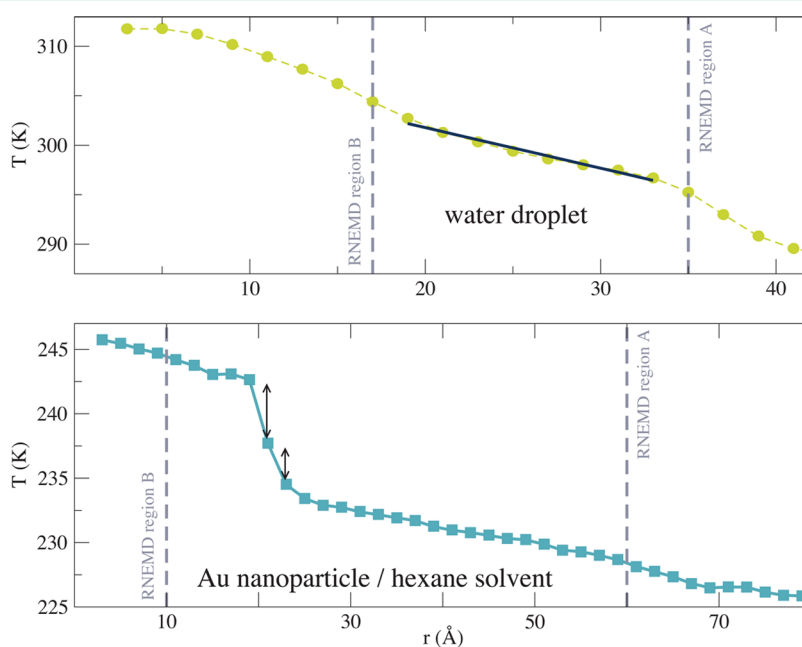


Figure 2. Upper panel: temperature profile of a typical SPC/E water droplet. The RNEMD simulation transfers kinetic energy from region A to region B, and the system responds by creating a temperature gradient (circles). The fit to determine $\langle dT/dr \rangle$ is carried out between the two RNEMD exchange regions. Lower panel: temperature profile for a solvated Au nanoparticle ($r = 20$ Å). The temperature differences used to compute the total Kapitza resistance (and interfacial thermal conductance) are indicated with arrows.

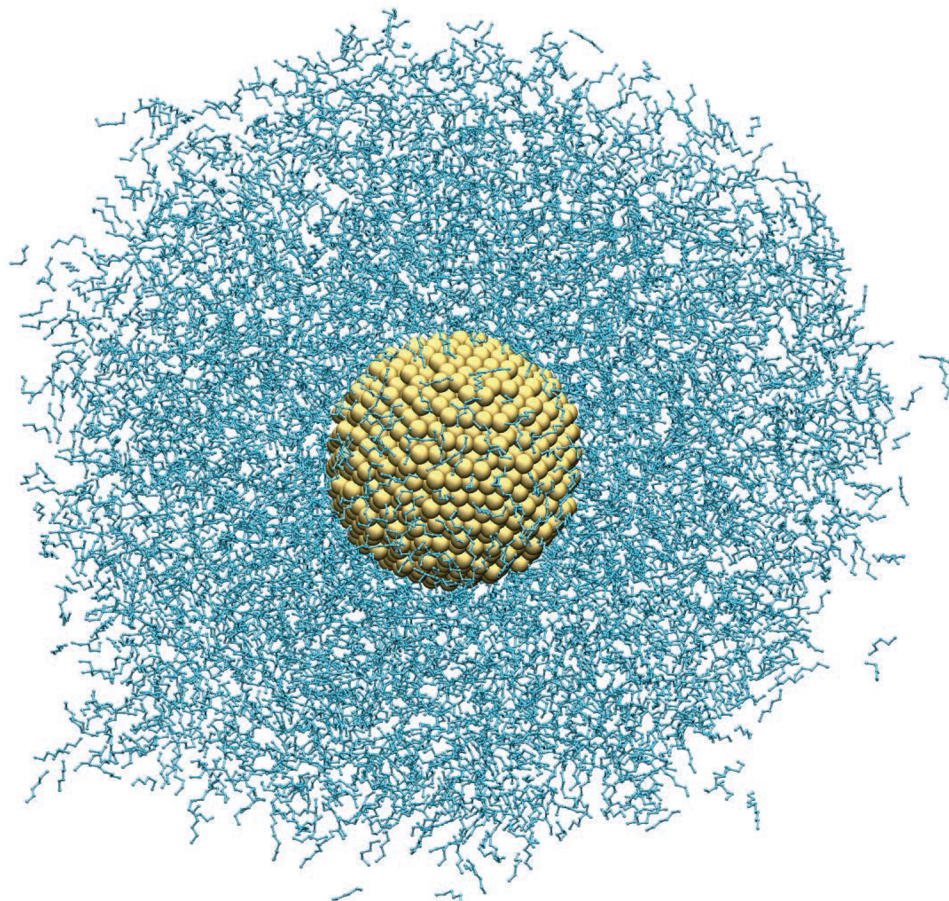


Figure 3. Gold nanoparticle with a radius of 20 Å solvated in TraPPE-UA hexane. A kinetic energy flux is applied between the nanoparticle and an outer shell of solvent to obtain the interfacial thermal conductance, G , and the interfacial rotational resistance, Ξ^r , is determined using an angular momentum flux.

To model the thermal conductance across a wide interface (or multiple interfaces), it is useful to consider concentric shells as resistors wired in series. The resistance of the shells is then additive, and the interfacial thermal conductance is the inverse of the total Kapitza resistance:

$$\frac{1}{G} = R_{\text{total}} = \frac{1}{q_r} \sum_i 4\pi r_i^2 (T_{i+1} - T_i) \quad (13)$$

This series can be extended for any number of adjacent shells, allowing for the calculation of the interfacial thermal conductance for interfaces of considerable thickness, such as self-assembled ligand monolayers on a metal surface.

3.4.1. Interfacial Thermal Conductance of Solvated Gold Nanoparticles. Calculated interfacial thermal conductance (G) values for three sizes of gold nanoparticles and a flat Au(111) surface solvated in TraPPE-UA hexane²³ are shown in Table 2.

The introduction of surface curvature increases the interfacial thermal conductance by a factor of approximately 1.5 relative to the flat interface, although there is no apparent size dependence in the G values obtained from our calculations. This is quite different behavior than the size dependence observed by Lervik et al.²⁴ in their NEMD simulations of decane droplets in water. In the liquid/liquid case, the surface tension is strongly dependent on the droplet size, and the interfacial resistivity increases with surface tension. In our case, the surface tension of the solid/liquid interface does not have a strong dependence on the particle radius at these particle sizes.

Table 2. Calculated Interfacial Thermal Conductance (G) Values for Gold Nanoparticles of Varying Radii Solvated in TraPPE-UA Hexane^a

nano particle radius (Å)	G (MW/(m ² ·K))
20	47.1 ± 5.0
30	45.4 ± 1.2
40	46.5 ± 2.1
Au(111)	30.2

^aThe nanoparticle G values are compared to previous simulation results for a Au(111) interface in TraPPE-UA hexane.

Simulations of larger nanoparticles may yet demonstrate limiting G values close to the flat Au(111) slab, although any spherical particle will have a significant fraction of the surface atoms in non-111 facets. It is not clear at this point whether the increase in thermal conductance for the spherical particles is due to the increased population of undercoordinated surface atoms or to increased solid angle space available for phonon scattering into the solvent. These two possibilities do open up some interesting avenues for investigation.

3.5. Interfacial Rotational Friction. The interfacial rotational resistance tensor, Ξ^r , can be calculated for heterogeneous nanostructure/solvent systems by applying an angular momentum flux between the solvated nanostructure and a spherical shell of solvent at the outer edge of the cluster.

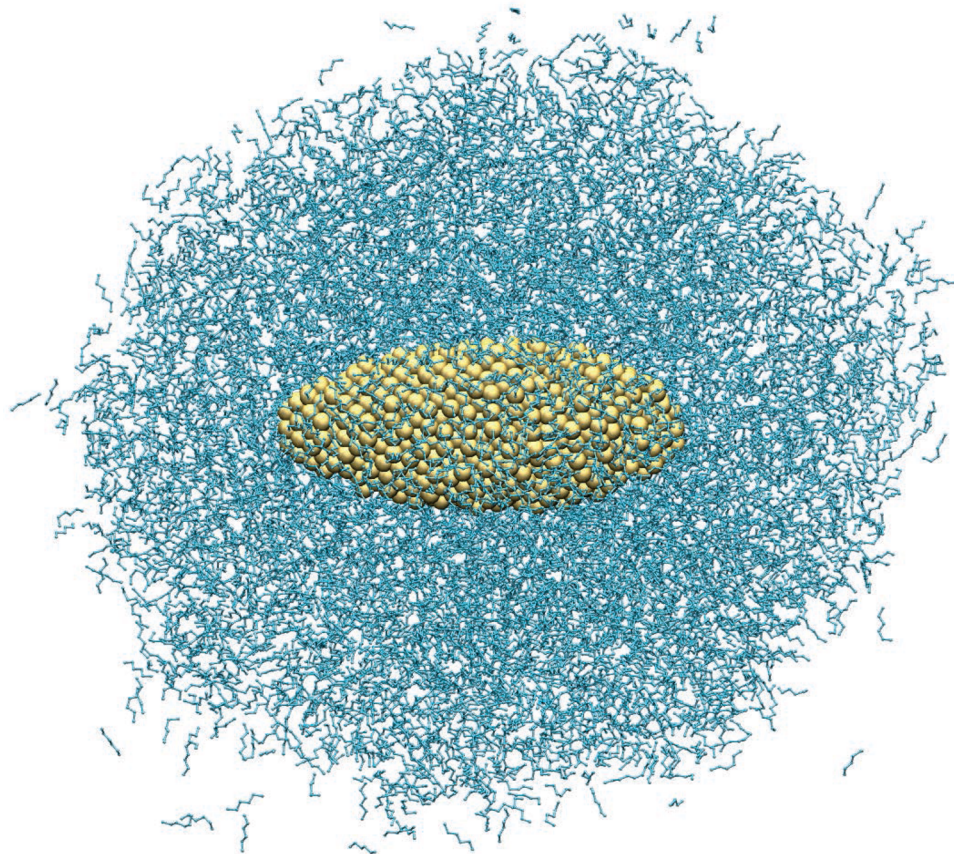


Figure 4. Gold prolate ellipsoid of length 65 Å and width 25 Å solvated by TraPPE-UA hexane. An angular momentum flux is applied between the ellipsoid and an outer shell of solvent.

An angular velocity gradient develops in response to the applied flux, causing the nanostructure and solvent shell to rotate in opposite directions about a given axis.

Analytical solutions for the diagonal elements of the rotational resistance tensor for a solvated spherical body of radius r under ideal stick boundary conditions can be estimated using Stokes' law

$$\Xi_{\text{stick}}^{\text{rr}} = 8\pi\eta r^3 \quad (14)$$

where η is the dynamic viscosity of the surrounding solvent.

For general ellipsoids with semiaxes α , β , and γ , Perrin's extension of Stokes' law provides exact solutions for symmetric prolate ($\alpha \geq \beta = \gamma$) and oblate ($\alpha < \beta = \gamma$) ellipsoids under ideal stick conditions.^{39,40} The Perrin elliptic integral parameter is

$$S = \frac{2}{\sqrt{\alpha^2 - \beta^2}} \ln \left[\frac{\alpha + \sqrt{\alpha^2 - \beta^2}}{\beta} \right] \quad (15)$$

For a prolate ellipsoidal nanoparticle (see Figure 4), the rotational resistance tensor Ξ^{rr} is a 3×3 diagonal matrix with elements

$$\Xi_{\alpha}^{\text{rr}} = \frac{32\pi}{3}\eta \frac{(\alpha^2 - \beta^2)\beta^2}{2\alpha - \beta^2 S} \quad (16)$$

$$\Xi_{\beta,\gamma}^{\text{rr}} = \frac{32\pi}{3}\eta \frac{(\alpha^4 - \beta^4)}{(2\alpha^2 - \beta^2)S - 2\alpha} \quad (17)$$

corresponding to rotation about the long axis (α), and each of the equivalent short axes (β and γ), respectively.

Previous VSS-RNEMD simulations of the interfacial friction of the planar Au(111)/hexane interface have shown that the flat interface exists within slip boundary conditions.²² Hu and Zwanzig⁴¹ investigated the rotational friction coefficients for spheroids under slip boundary conditions and obtained numerical results for a scaling factor to be applied to $\Xi_{\text{stick}}^{\text{rr}}$ as a function of the ratio of the shorter semiaxes to the longer. Under slip conditions, rotation of any sphere and rotation of a prolate ellipsoid about its long axis does not displace any solvent, so the resulting $\Xi_{\text{slip}}^{\text{rr}}$ approaches 0. For rotation of a prolate ellipsoid (with the aspect ratio shown here) about its short axis, Hu and Zwanzig obtained $\Xi_{\text{slip}}^{\text{rr}}$ values of 35.9% of the analytical $\Xi_{\text{stick}}^{\text{rr}}$ result. This reduced rotational resistance accounts for the reduced interfacial friction under slip boundary conditions.

The simulated rotational friction coefficient, $\Xi_{\text{sim}}^{\text{rr}}$, at the interface can be extracted from nonperiodic VSS-RNEMD simulations quite easily using the total applied torque (τ) and the observed angular velocity of the solid structure (ω_{solid}),

$$\Xi_{\text{sim}}^{\text{rr}} = \frac{\tau}{\omega_{\text{solid}}} \quad (18)$$

The total applied torque required to overcome the interfacial friction and maintain constant angular rotation of the solid particle is

$$\tau = \frac{j_r(\mathbf{L}) \cdot \mathbf{A}}{2} \quad (19)$$

Table 3. Comparison of Rotational Friction Coefficients under Ideal Stick ($\Xi_{\text{stick}}^{\text{rr}}$) and Slip ($\Xi_{\text{slip}}^{\text{rr}}$) Conditions, Along with the Simulated ($\Xi_{\text{sim}}^{\text{rr}}$) rotational Friction Coefficients of Gold Nanostructures Solvated in TraPPE-UA Hexane at 230 K^a

structure	axis of rotation	$\Xi_{\text{stick}}^{\text{rr}}$ (amu A ² /fs)	$\Xi_{\text{slip}}^{\text{rr}}$ (amu A ² /fs)	$\Xi_{\text{sim}}^{\text{rr}}$ (amu A ² /fs)	$\Xi_{\text{sim}}^{\text{rr}}/\Xi_{\text{stick}}^{\text{rr}}$
sphere ($r = 20 \text{ \AA}$)	$x = y = z$	3314	0	2386 ± 14	0.720 ± 0.004
sphere ($r = 30 \text{ \AA}$)	$x = y = z$	11 749	0	8415 ± 274	0.716 ± 0.023
sphere ($r = 40 \text{ \AA}$)	$x = y = z$	34 464	0	47544 ± 3051	1.380 ± 0.089
prolate ellipsoid	$x = y$	4991	1792	3128 ± 166	0.627 ± 0.033
prolate ellipsoid	z	1993	0	1590 ± 30	0.798 ± 0.015

^aThe ellipsoid is oriented with the long axis along the z direction.

where $j_r(L)$ is the applied angular momentum flux, A is the surface area of the solid nanoparticle, and the factor of 2 is present because the torque is exerted on both the particle and the counter-rotating solvent shell.

3.5.1. Rotational Friction for Gold Nanostructures in Hexane. Table 3 shows the calculated rotational friction coefficients Ξ^{rr} for spherical gold nanoparticles and a prolate ellipsoidal gold nanorod solvated in TraPPE-UA hexane. An angular momentum flux was applied between an outer shell of solvent that was at least 20 Å away from the surface of the particle (region A) and the gold nanostructure (region B). Dynamic viscosity estimates (η) for TraPPE-UA hexane under these particular temperature and pressure conditions were determined by applying a traditional VSS-RNEMD linear momentum flux to a periodic box of this solvent.

The results for $\Xi_{\text{sim}}^{\text{rr}}$ show that, in contrast with the flat Au(111)/hexane interface, gold nanostructures solvated by hexane are closer to stick than slip boundary conditions. At these length scales, the nanostructures are not perfect spheroids due to atomic “roughening” of the surface and therefore experience increased interfacial friction, deviating significantly from the ideal slip case. The 20 and 30 Å radius nanoparticles experience approximately 70% of the ideal stick boundary interfacial friction. Rotation of the ellipsoid about its long axis more closely approaches the stick limit than rotation about the short axis, which at first seems counterintuitive. However, the “propeller” motion caused by rotation around the short axis may exclude solvent from the rotation cavity or move a sufficient amount of solvent along with the gold that a smaller interfacial friction is actually experienced.

The largest nanoparticle (40 Å radius) appears to experience interfacial friction in excess of ideal stick conditions. Although the solvent velocity field does not appear in the calculation of Ξ^{rr} , we do note that the smaller particles exhibit solvent velocity fields that can be fit with the $v(r,\theta) = \sin \theta (Ar + B/r^2)$ form first discovered by Jeffery,⁴² while the solvent velocity fields for the $r = 40 \text{ \AA}$ particle approaches the infinite fluid solution and can be fit well with only the second term. The larger particle (and the resulting larger solvent volume) appears to be transitioning to a regime that approaches the infinite solvent solutions.

4. DISCUSSION

We have adapted the VSS-RNEMD methodology so that it can be used to apply kinetic energy and angular momentum fluxes in explicitly nonperiodic simulation geometries. Nonperiodic VSS-RNEMD preserves the strengths of the original periodic variant, specifically Boltzmann velocity distributions and minimal thermal anisotropy, while extending the constraints to conserve total energy and total angular momentum. This method also maintains the ability to impose the kinetic energy and angular momentum fluxes either jointly or individually.

This method enables steady-state calculation of interfacial thermal conductance and interfacial rotational friction in heterogeneous clusters. We have demonstrated the abilities of the method on some familiar systems (nanocrystalline gold, SPC/E water) as well as on interfaces that have been studied only in planar geometries. For the bulk systems that are well-understood in periodic geometries, the nonperiodic VSS-RNEMD provides very similar estimates of the thermal conductivity to other simulation methods.

For nanoparticle-to-solvent heat transfer, we have observed that the interfacial conductance exhibits a 1.5 times increase over the planar Au(111) interface, although we do not see any dependence of the conductance on the particle size. Because the surface tension effects present in liquid/liquid heat transfer are not strong contributors here, we suggest two possible mechanisms for the 1.5 times increase over the planar surface: (1) the nanoparticles have an increased population of undercoordinated surface atoms that are more efficient at transferring vibrational energy to the solvent, or (2) there is increased solid angle space available for phonon scattering into the solvent. The second of these explanations would have a significant dependence on the radius of spherical particles, although crystalline faceting of the particles may be enough to reduce this dependence on particle radius. These two possibilities open up some interesting avenues for further exploration.

One area that this method opens up that was not available for periodic simulation cells is direct computation of the solid/liquid rotational friction coefficients of nanostructures. The systems we have investigated (gold nanospheres and prolate ellipsoids) have analytic stick and numerical slip solutions provided via hydrodynamics, and our molecular simulations indicate that the bare metallic nanoparticles are closer to stick than they are to slip conditions. This is markedly different behavior than we have seen for the solid/liquid friction at planar Au(111) interfaces in previous simulations, where the solvents experience a nearly laminar flow over the surface.

Schmidt and Skinner previously computed the behavior of spherical tag particles in molecular dynamics simulations and showed that *slip* boundary conditions for translational resistance may be more appropriate for molecule-sized spheres embedded in a sea of spherical solvent particles.^{43,44} The size of the gold nanoparticles studied here and the structuring of the particle surfaces appear to bring the behavior closer to stick boundaries.

Rotational correlation times of roughened spheres in explicit solvent were also investigated using equilibrium molecular dynamics by Heyes et al.⁴⁵ who found that rotational diffusion of the rough spheres exhibits effective solvent viscosities that are significantly below the bulk viscosity. From this they concluded that the rate of rotation is faster than predicted using classical Stokes–Einstein stick boundary conditions. This is

consistent with our observations for the smaller nanoparticles. The effect observed by Heyes et al. disappears or reverses for larger spheres in higher density solvents. This is consistent with our observations for the 40 Å nanoparticles.

Sun et al. have carried out equilibrium MD simulations on smooth ellipsoids and rigid dumbbell shapes in an explicit solvent.⁴⁶ They observed slower than stick boundary predictions for the rotational motion of the smooth ellipsoid but significantly faster than stick behavior for the roughened surface of the rigid dumbbell. Because our gold ellipsoids are relatively rough atomic surfaces, we appear to be closer to the dumbbell behavior than the smooth ellipsoid.

Exactly where the slip–stick crossover takes place for the spheres is an interesting avenue for future exploration. The ability to interrogate nonperiodic effects (e.g., surface curvature, edge effects between facets, and the splay of ligand surface groups) on interfacial transport means that this method can be applied to systems of broad experimental and theoretical interest.

AUTHOR INFORMATION

Corresponding Author

*E-mail: gezelter@nd.edu.

Notes

The authors declare no competing financial interest.

ACKNOWLEDGMENTS

We thank Dr. Shenyu Kuang for helpful discussions. Support for this project was provided by the National Science Foundation under Grant CHE-0848243. Computational time was provided by the Center for Research Computing (CRC) at the University of Notre Dame.

REFERENCES

- (1) Ashurst, W. T.; Hoover, W. G. Dense-Fluid Shear Viscosity via Nonequilibrium Molecular Dynamics. *Phys. Rev. A* **1975**, *11*, 658–678.
- (2) Evans, D. J. Homogeneous NEMD Algorithm for Thermal Conductivity—Application of Non-Canonical Linear Response Theory. *Phys. Lett. A* **1982**, *91*, 457–460.
- (3) Erpenbeck, J. J. Shear Viscosity of the Hard-Sphere Fluid via Nonequilibrium Molecular Dynamics. *Phys. Rev. Lett.* **1984**, *52*, 1333–1335.
- (4) Evans, D. J. Thermal Conductivity of the Lennard-Jones Fluid. *Phys. Rev. A* **1986**, *34*, 1449–1453.
- (5) Vogelsang, R.; Hoheisel, G.; Luckas, M. Shear Viscosity and Thermal Conductivity of the Lennard-Jones Liquid Computed Using Molecular Dynamics and Predicted by a Memory Function Model for a Large Number of States. *Mol. Phys.* **1988**, *64*, 1203–1213.
- (6) Maginn, E. J.; Bell, A. T.; Theodorou, D. N. Transport Diffusivity of Methane in Silicalite from Equilibrium and Nonequilibrium Simulations. *J. Phys. Chem.* **1993**, *97*, 4173–4181.
- (7) Hess, B. Determining the Shear Viscosity of Model Liquids from Molecular Dynamics Simulations. *J. Chem. Phys.* **2002**, *116*, 209–217.
- (8) Schelling, P. K.; Phillpot, S. R.; Kebinski, P. Comparison of Atomic-Level Simulation Methods for Computing Thermal Conductivity. *Phys. Rev. B* **2002**, *65*, 144306.
- (9) Berthier, L.; Barrat, J. L. Nonequilibrium Dynamics and Fluctuation-Dissipation Relation in a Sheared Fluid. *J. Chem. Phys.* **2002**, *116*, 6228–6242.
- (10) Evans, D. J.; Searles, D. J. The Fluctuation Theorem. *Adv. Phys.* **2002**, *51*, 1529–1585.
- (11) Vasquez, V. R.; Macedo, E. A.; Zabaloy, M. S. Lennard-Jones Viscosities in Wide Ranges of Temperature and Density: Fast Calculations Using a Steady-State Periodic Perturbation Method. *Int. J. Thermophys.* **2004**, *25*, 1799–1818.
- (12) Backer, J. A.; Lowe, C. P.; Hoefsloot, H. C. J.; Iedema, P. D. Poiseuille Flow to Measure the Viscosity of Particle Model Fluids. *J. Chem. Phys.* **2005**, *122*, 154503.
- (13) Jiang, H.; Myshakin, E. M.; Jordan, K. D.; Warzinski, R. P. Molecular Dynamics Simulations of the Thermal Conductivity of Methane Hydrate. *J. Phys. Chem. B* **2008**, *112*, 10207–10216.
- (14) Picalek, J.; Kolafa, J. Shear Viscosity of Ionic Liquids from Non-Equilibrium Molecular Dynamics Simulation. *Mol. Simul.* **2009**, *35*, 685–690.
- (15) Müller-Plathe, F. A Simple Nonequilibrium Molecular Dynamics Method for Calculating the Thermal Conductivity. *J. Chem. Phys.* **1997**, *106*, 6082–6085.
- (16) Müller-Plathe, F. Reversing the Perturbation in Nonequilibrium Molecular Dynamics: An Easy Way to Calculate the Shear Viscosity of Fluids. *Phys. Rev. E* **1999**, *59*, 4894–4898.
- (17) Patel, H. A.; Garde, S.; Kebinski, P. Thermal Resistance of Nanoscopic Liquid-Liquid Interfaces: Dependence on Chemistry and Molecular Architecture. *Nano Lett.* **2005**, *5*, 2225–2231.
- (18) Shenogina, N.; Godawat, R.; Kebinski, P.; Garde, S. How Wetting and Adhesion Affect Thermal Conductance of a Range of Hydrophobic to Hydrophilic Aqueous Interfaces. *Phys. Rev. Lett.* **2009**, *102*, 156101.
- (19) Tenney, C. M.; Maginn, E. J. Limitations and Recommendations for the Calculation of Shear Viscosity using Reverse Nonequilibrium Molecular Dynamics. *J. Chem. Phys.* **2010**, *132*, 014103.
- (20) Kuang, S.; Gezelter, J. D. A Gentler Approach to RNEMD: Nonisotropic Velocity Scaling for Computing Thermal Conductivity and Shear Viscosity. *J. Chem. Phys.* **2010**, *133*, 164101-1–164101-9.
- (21) Kuang, S.; Gezelter, J. D. Simulating Interfacial Thermal Conductance at Metal-Solvent Interfaces: The Role of Chemical Capping Agents. *J. Phys. Chem. C* **2011**, *115*, 22475–22483.
- (22) Kuang, S.; Gezelter, J. D. Velocity Shearing and Scaling RNEMD: A Minimally Perturbing Method for Simulating Temperature and Momentum Gradients. *Mol. Phys.* **2012**, *110*, 691–701.
- (23) Stocker, K. M.; Gezelter, J. D. Simulations of Heat Conduction at Thiolate-Capped Gold Surfaces: The Role of Chain Length and Solvent Penetration. *J. Phys. Chem. C* **2013**, *117*, 7605–7612.
- (24) Lervik, A.; Bresme, F.; Kjelstrup, S. Heat Transfer in Soft Nanoscale Interfaces: The Influence of Interface Curvature. *Soft Matter* **2009**, *5*, 2407–2414.
- (25) Alaghemandi, M.; Müller-Plathe, F.; Böhm, M. C. Thermal conductivity of carbon nanotube—polyamide-6,6 nanocomposites: Reverse non-equilibrium molecular dynamics simulations. *J. Chem. Phys.* **2011**, *135*, 184905-1–184905-9.
- (26) Vardeman, C. F.; Stocker, K. M.; Gezelter, J. D. The Langevin Hull: Constant Pressure and Temperature Dynamics for Nonperiodic Systems. *J. Chem. Theory Comput.* **2011**, *7*, 834–842.
- (27) Meineke, M. A.; Vardeman, C. F.; Lin, T.; Fennell, C.; Gezelter, J. D. OOPSE: An Object-Oriented Parallel Simulation Engine for Molecular Dynamics. *J. Comput. Chem.* **2005**, *26*, 252–271.
- (28) Gezelter, J. D.; Kuang, S.; Marr, J.; Stocker, K.; Li, C.; Vardeman, C. F.; Lin, T.; Fennell, C. J.; Sun, X.; Daily, K.; Zheng, Y.; Meineke, M. A. OpenMD, An open source molecular dynamics engine, version 2.1; <http://openmd.org> (accessed Nov. 13, 2013).
- (29) Qi, Y.; Çağın, T.; Kimura, Y.; Goddard, W. A., III. Molecular-Dynamics Simulations of Glass Formation and Crystallization in Binary Liquid Metals: Cu-Ag and Cu-Ni. *Phys. Rev. B* **1999**, *59*, 3527–3533.
- (30) Berendsen, H. J. C.; Grigera, J. R.; Straatsma, T. P. The Missing Term in Effective Pair Potentials. *J. Phys. Chem.* **1987**, *91*, 6269–6271.
- (31) Bedrov, D.; Smith, G. Thermal Conductivity of Molecular Fluids from Molecular Dynamics Simulations: Application of a New Imposed-Flux Method. *J. Chem. Phys.* **2000**, *113*, 8080–8084.
- (32) Martin, M. G.; Siepmann, J. I. Transferable Potentials for Phase Equilibria. 1. United-Atom Description of *n*-Alkanes. *J. Phys. Chem. B* **1998**, *102*, 2569–2577.
- (33) Schapotschnikow, P.; Pool, R.; Vlugt, T. J. Selective Adsorption of Alkyl Thiols on Gold in Different Geometries. *Comput. Phys. Commun.* **2007**, *177*, 154–157.

- (34) Hautman, J.; Klein, M. L. Simulation of a Monolayer of Alkyl Thiol Chains. *J. Chem. Phys.* **1989**, *91*, 4994–5001.
- (35) Martínez, L.; Andrade, R.; Birgin, E. G.; Martínez, J. M. PACKMOL: A Package for Building Initial Configurations for Molecular Dynamics Simulations. *J. Comput. Chem.* **2009**, *30*, 2157–2164.
- (36) Zhang, M.; Lussetti, E.; de Souza, L.; Müller-Plathe, F. Thermal Conductivities of Molecular Liquids by Reverse Nonequilibrium Molecular Dynamics. *J. Phys. Chem. B* **2005**, *109*, 15060–15067.
- (37) Römer, F.; Lervik, A.; Bresme, F. Nonequilibrium Molecular Dynamics Simulations of the Thermal Conductivity of Water: A Systematic Investigation of the SPC/E and TIP4P/2005 Models. *J. Chem. Phys.* **2012**, *137*, 074503-1–074503-8.
- (38) Wagner, W.; Kruse, A. *Properties of Water and Steam, the Industrial Standard IAPWS-IF97 for the Thermodynamic Properties and Supplementary Equations for Other Properties*; Springer-Verlag: Berlin, 1998.
- (39) Perrin, F. Mouvement Brownien d'un ellipsoid(I). Dispersion dielectrique pour des molecules ellipsoidales. *J. Phys. Radium* **1934**, *5*, 497–511.
- (40) Perrin, F. Mouvement Brownien d'un ellipsoid(II). Rotation libre et depolarisation des fluorescences. Translation et diffusion de molecules ellipsoidales. *J. Phys. Radium* **1936**, *7*, 1–11.
- (41) Hu, C.; Zwanzig, R. Rotational Friction Coefficients for Spheroids with the Slipping Boundary Condition. *J. Chem. Phys.* **1974**, *60*, 4353–4357.
- (42) Jeffery, G. B. On the Steady Rotation of a Solid of Revolution in a Viscous Fluid. *Proc. London Math. Soc.* **1915**, *2_14*, 327–338.
- (43) Schmidt, J.; Skinner, J. Brownian Motion of a Rough Sphere and the Stokes–Einstein Law. *J. Phys. Chem. B* **2004**, *108*, 6767–6771.
- (44) Schmidt, J.; Skinner, J. Hydrodynamic Boundary Conditions, the Stokes-Einstein Law, and Long-Time Tails in the Brownian Limit. *J. Chem. Phys.* **2003**, *119*, 8062–8068.
- (45) Heyes, D. M.; Nuevo, M. J.; Morales, J. J. Translational and rotational diffusion of dilute solid amorphous spherical nanocolloids by molecular dynamics simulation. *Mol. Phys.* **1998**, *93*, 985–994.
- (46) Sun, X.; Lin, T.; Gezelter, J. D. Langevin Dynamics for Rigid Bodies of Arbitrary Shape. *J. Chem. Phys.* **2008**, *128*, 234107.